

Physics-based generation of multilayer corneal OCT data via Gaussian modeling and MCML for AI-driven diagnostic and surgical guidance applications

Jinglun Yu^a, Yaning Wang^a, Rosalinda Xiong^a, Ziyi Huang^a, Kristina Irsch^{b,c}, and Jin U. Kang^a

^aDepartment of Electrical and Computer Engineering,
Johns Hopkins University, Baltimore, MD 21218, USA

^bWilmer Eye Institute, Johns Hopkins University, Baltimore, MD 21287, USA

^cVision Institute, Sorbonne University, INSERM, CNRS, Paris, France

ABSTRACT

Training deep learning models for corneal optical coherence tomography (OCT) imaging is limited by the availability of large, well-annotated datasets. We present a configurable Monte Carlo simulation framework that generates synthetic corneal B-scan optical OCT images with pixel-level five-layer segmentation labels derived directly from the simulation geometry. A five-layer corneal model with Gaussian surfaces captures curvature and thickness variability in healthy and keratoconic eyes. Each layer is assigned optical properties from the literature and light transport is simulated using Monte Carlo modeling of light transport in multi-layered tissues (MCML), while incorporating system features such as the confocal PSF and sensitivity roll-off. This approach produces over 10,000 high-resolution (1024×1024) image-label pairs and supports customization of geometry, photon count, noise, and system parameters. The resulting dataset enables systematic training, validation, and benchmarking of AI models under controlled, ground-truth conditions, providing a reproducible and scalable resource to support the development of diagnostic and surgical guidance applications in image-guided ophthalmology.

Keywords: Synthetic OCT data, Monte Carlo modeling of light, OCT corneal imaging, Gaussian modeling, AI benchmark generation

1. INTRODUCTION

Corneal OCT is a cornerstone modality for diagnosing anterior-segment disease and enabling image-guided ophthalmic procedures,^{1,2} but data availability remains a major bottleneck for AI. Large-scale corneal B-scan collections are hard to curate because clinical data are privacy-sensitive, acquisition protocols vary across devices, and consistent multilayer annotations are costly to produce. This limitation is especially acute in surgery-adjacent settings—such as penetrating keratoplasty (PK) and deep anterior lamellar keratoplasty (DALK)^{3–6}—where layer-aware interpretation can support intraoperative decision-making and reduce uncertainty in depth-critical maneuvers.⁷ Pixel-level multilayer annotation is labor-intensive, and small datasets rarely capture the full variability of healthy and keratoconic corneas, as well as speckle and system-dependent artifacts. Data scarcity also limits the feasibility of data-hungry generative approaches (e.g., diffusion models) for augmentation or representation learning. Meanwhile, early-stage development for corneal enhancement tasks—such as super-resolution,^{8,9} denoising, and domain adaptation—often relies on *ex vivo* animal-eye data. While valuable, these data can differ from human corneal geometry and optical properties,¹⁰ limiting their ability to support systematic robustness testing. A controllable, human-cornea-like synthetic resource could therefore provide scalable training data and enable stress-testing under known, parameterized perturbations.

Given the limited availability of large, finely annotated OCT datasets, recent work uses synthetic data in two main ways. Learning-based generators (GANs/diffusion) can expand training sets or balance classes,^{11,12} but

Further author information: (Send correspondence to Jinglun Yu)
Jinglun Yu: E-mail: jyu146@jhu.edu

image realism alone does not guarantee anatomically consistent layers or pixel-aligned masks, often requiring additional heuristics to derive labels.¹⁰ Physics-based simulators provide controllable, self-consistent supervision, yet face fidelity–efficiency trade-offs: wave-equation models are costly at clinical scale, while simplified models can miss scattering and system effects.¹³ Many Monte Carlo OCT simulators further prioritize A-scan settings or constrained geometries, limiting scalable high-resolution B-scan synthesis with flexible anatomy and “label-perfect” multilayer masks.¹⁴

Here we present a configurable, parallel physics-based framework that generates high-resolution synthetic corneal OCT B-scans with exact multilayer ground truth. We construct a five-layer cornea using Gaussian surface profiles to model anatomically plausible curvature and thickness variability spanning healthy and keratoconic phenotypes, and assign literature-based optical properties per layer. OCT signal formation is simulated with Monte Carlo modeling of light transport in multi-layered tissues (MCML),¹⁵ augmented with confocal PSF gating and sensitivity roll-off to capture key system effects under controlled perturbations.¹⁶ Because geometry and parameters are explicitly defined, pixel-aligned five-layer masks are exported automatically with perfect correspondence. The pipeline produces $>10,000$ paired 1024×1024 image–label samples and supports systematic sweeps over curvature, thickness, photon count, noise, and PSF variants for reproducible benchmarking and robustness testing.

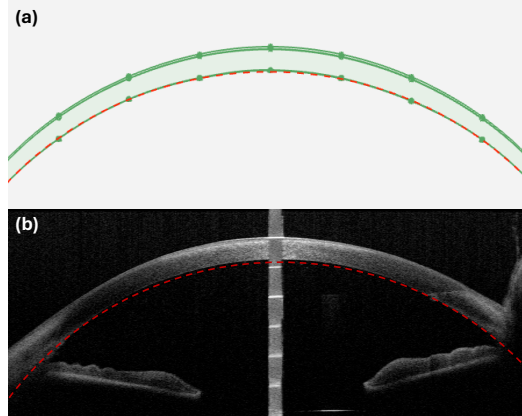


Figure 1. (a) Semi-circular baseline curvature used as the first-order corneal support profile (red dashed curve). (b) Clinical corneal OCT B-scan with the fitted semi-circular baseline overlaid (red dashed curve) to illustrate dome-shape consistency. Panel (b) is from the public dataset <https://doi.org/10.6084/m9.figshare.25952845>¹⁷ and was cropped and annotated for visualization.

2. METHODS

2.1 Gaussian-Based Multilayer Corneal Geometry Modeling

2.1.1 Boundary Parameterization and Random Sampling

An anatomically plausible corneal B-scan geometry with controllable variability is generated by modeling each corneal layer boundary as a smooth 2D curve along the lateral axis x . A global baseline curvature is first defined using a semi-circular support profile,

$$y_{\text{base}}(x) = R - \sqrt{R^2 - x^2}, \quad (1)$$

which captures the dome-shaped corneal curvature and provides a physically interpretable first-order fit to the dome-shaped corneal boundary and is visually validated against a representative clinical B-scan in Fig. 1. A parameterized sinusoidal–Gaussian deformation is applied to the baseline surface, enabling keratoconus-like cone formation via localized steepening (Figure 2 shows an example of simulated healthy and keratoconus-like corneas). The deformation is defined as

$$\Delta y(x) = A_1 \cos\left(\frac{f_1 \pi (x + D)}{R}\right) + A_2 \sin\left(\frac{f_2 \pi (x + D)}{R}\right) + H \exp\left(-\frac{(x - x_0)^2}{2\sigma^2}\right), \quad (2)$$

and the resulting boundary is given by

$$y(x) = y_{\text{base}}(x) + \Delta y(x). \quad (3)$$

Here, (A_1, f_1) and (A_2, f_2) control low- and high-frequency components, D introduces lateral offset (decentering), and the Gaussian term (H, x_0, σ) controls the height, location, and width of a localized bulge. Randomness is introduced by sampling R , D , x_0 , (A_1, A_2, H) , (f_1, f_2) , and σ on a per-sample basis within bounded, physiologically feasible ranges (implemented as small perturbations around nominal values), enabling controlled sweeps over anatomical variability while maintaining smooth and realistic curvature. A fixed random seed can optionally be used to reproduce identical geometries across runs.

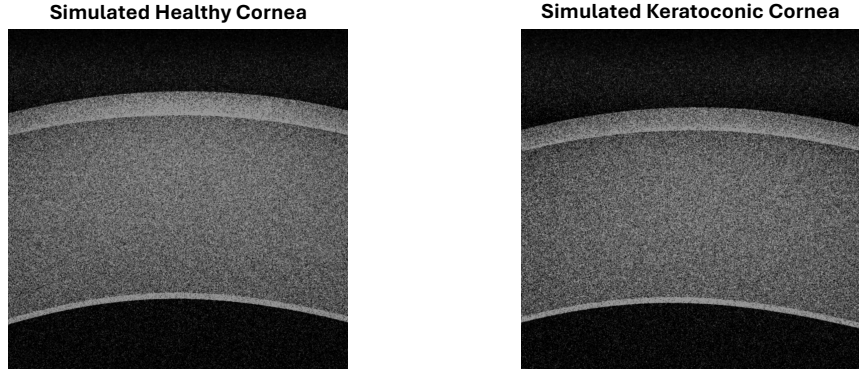


Figure 2. Representative simulated corneal OCT B-scans generated by our model: a healthy cornea (left) and a keratoconic cornea (right), where a localized anterior steepening is introduced to mimic keratoconus-like morphology.

2.1.2 Multilayer Model Construction and Calibration

A five-layer cornea (epithelium, Bowman's layer, stroma, Descemet's membrane, and endothelium) is constructed by stacking boundaries with independently controlled thickness profiles, as illustrated in Fig. 3. Given an initial boundary $y_0(x)$, subsequent interfaces are generated as

$$y_{k+1}(x) = y_k(x) + t_k(x), \quad (4)$$

where $t_k(x)$ denotes the thickness of layer k . Inter-sample variability is introduced by applying a unified multiplicative perturbation to nominal profiles,

$$t_k(x) = s t_k^{(0)}(x), \quad s \sim \mathcal{U}(1 - \delta, 1 + \delta), \quad \delta = 0.05 - 0.10, \quad (5)$$

followed by adaptive constraint enforcement: if any boundary overlap or ordering violation occurs, the perturbation is damped (i.e., s is reduced) until all interfaces remain non-intersecting and layer-specific lower bounds are satisfied.

To match clinical B-scan metrics and standard OCT visualization, the geometry is rendered with a calibrated lateral–axial aspect ratio. As shown in Fig. 4, the multilayer region is then cropped to a central, clinically relevant window before forward simulation and label rasterization and an axial scaling relative to the lateral axis ($Z/X \approx 1/3$) is applied to preserve clinically meaningful curvature and layer spacing, anchored to representative scan widths.

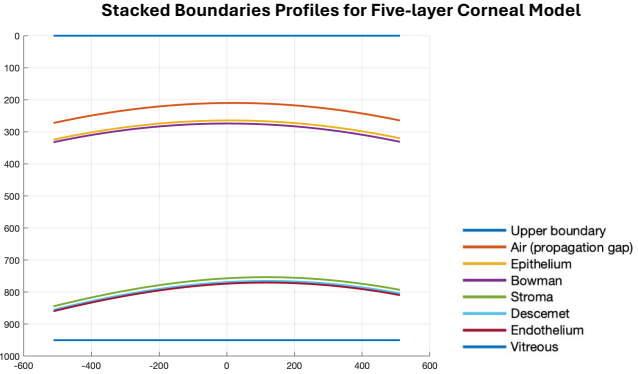


Figure 3. Stacked boundaries profiles used to construct a five-layer corneal model. Each interface curve defines one layer boundary, enabling independent control of the thickness profiles for the epithelium, Bowman's layer, stroma, Descemet's membrane, and endothelium; the upper boundary, air (propagation gap), and vitreous boundary are included for completeness.

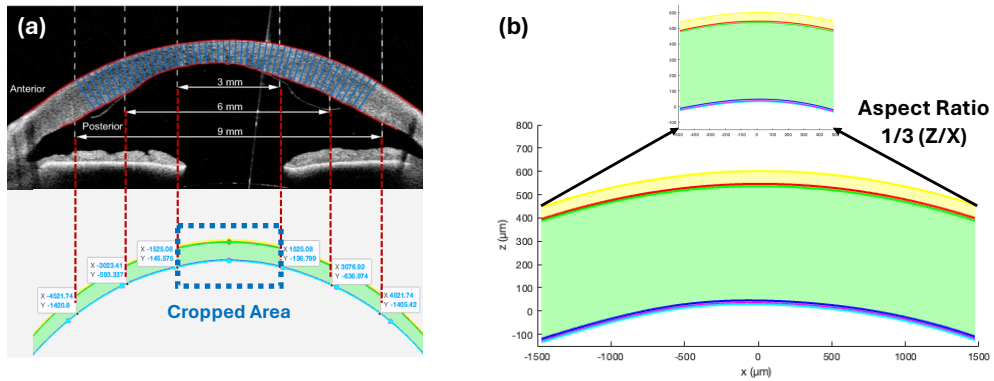


Figure 4. (a) Simulated cornea section anchored to clinically relevant scan widths (3–9 mm). The upper portion of panel (a) includes adapted material from Scientific Reports (DOI: 10.1038/s41598-021-93186-9) under CC BY 4.0¹⁸ and was re-rendered and annotated. (b) Cropped multilayer corneal area from panel (a) and the final calibrated visualization, obtained by applying the aspect-ratio.

2.2 Physics-Based OCT Forward Simulation via MCML

2.2.1 Optical Coefficient Specification and Map Generation

Layer-wise optical properties are specified under a piecewise-homogeneous assumption, where each anatomical layer is assigned constant refractive index n , absorption coefficient μ_a , scattering coefficient μ_s , and anisotropy factor g based on literature-reported values.^{19–23} The coefficients used in this work are summarized in Table 1. The column d reports the nominal (average) layer thickness in centimeters for reference.

For each simulated B-scan, the multilayer geometry is represented by ordered interfaces $\{y_k(x)\}_{k=1}^K$ (in μm) along the lateral coordinate x , where $K = 6$ corresponds to the six corneal boundaries and an additional bottom limit closes the simulation window. From these interfaces, a per-A-line layer-thickness map is computed via adjacent boundary differences,

$$\mathbf{t}(x) = [t_{\text{air}}(x), t_{\text{epi}}(x), t_{\text{bow}}(x), t_{\text{str}}(x), t_{\text{des}}(x), t_{\text{end}}(x), t_{\text{vit}}(x)]^\top, \quad (6)$$

with, for example, $t_{\text{epi}}(x) = y_{\text{air}}(x) - y_{\text{epi}}(x)$ and $t_{\text{bow}}(x) = y_{\text{epi}}(x) - y_{\text{bow}}(x)$. Thickness profiles are converted to centimeters for MCML input.¹⁴

Table 1. Layer-wise optical properties for MCML forward simulation (literature-based constants). The tear film (thickness $\approx 3\ \mu\text{m}$) is omitted and modeled implicitly via the air–epithelium interface. d is the nominal average layer thickness (cm) used in simulation.

Layer	n	μ_a (cm $^{-1}$)	μ_s (cm $^{-1}$)	g	d (cm)
Air (propagation gap)	1.000	0.00	0.00	0.00	0.0262
Epithelium	1.400	0.20	10.00	0.92	0.0052
Bowman	1.400	0.20	8.00	0.92	8.3612e-04
Stroma	1.376	0.20	4.50	0.94	0.0489
Descemet	1.375	0.30	8.00	0.93	0.0011
Endothelium	1.375	0.30	10.00	0.93	4.4537e-04
Vitreous Body	1.336	0.06	0.02	0.93	0.0124

A pixel-wise layer index map $L(x, z)$ is then derived by assigning each pixel at axial coordinate z (increasing downward in the rendered B-scan) to the unique layer interval bounded by adjacent interfaces:

$$L(x, z) = \ell \quad \text{if} \quad y_{\ell-1}(x) \geq z > y_\ell(x), \quad (7)$$

where $\ell \in \{1, \dots, 7\}$ denotes the layer (Air, Epithelium, …, Vitreous), and $y_0(x)$ and $y_7(x)$ denote the top and bottom limits of the cropped window, respectively. Given $L(x, z)$, coefficient maps are generated by piecewise-constant projection:

$$n(x, z) = n_{L(x, z)}, \quad \mu_a(x, z) = \mu_{a, L(x, z)}, \quad \mu_s(x, z) = \mu_{s, L(x, z)}, \quad g(x, z) = g_{L(x, z)}, \quad (8)$$

yielding pixel-aligned optical property maps exactly consistent with the sampled multilayer geometry.

2.2.2 MCML with Sensitivity Roll-off and Confocal Gating

The OCT forward model is implemented using the Monte Carlo simulation of photon transport in a multi-layer scattering medium parameterized by (μ_a, μ_s, g, n) per layer.¹⁶ Photon step lengths are sampled from an exponential distribution,

$$s = -\frac{\ln(\xi)}{\mu_t}, \quad \mu_t = \mu_a + \mu_s, \quad \xi \sim \mathcal{U}(0, 1), \quad (9)$$

with photon weight reduced according to the absorption fraction μ_a/μ_t at each interaction. Scattering directions are sampled from the Henyey–Greenstein phase function

$$f_{\text{HG}}(\cos \theta) = \frac{1 - g^2}{2(1 + g^2 - 2g \cos \theta)^{3/2}}, \quad (10)$$

using inverse-CDF sampling for θ and uniform sampling for the azimuthal angle. Boundary crossings are handled using Fresnel reflection/refraction based on refractive indices, and low-weight photons are terminated via Russian roulette. Detected photons are accumulated into a depth-resolved A-line $R(z, x)$.¹⁶

To approximate system-dependent OCT sensitivity, a parametric, implementation-level model is applied via depth-dependent confocal gating and sensitivity roll-off. Confocal weighting is modeled as a Gaussian envelope centered at the focal depth z_0 ,

$$W_{\text{conf}}(z) = \exp\left(-\frac{(z - z_0)^2}{2\sigma_c^2}\right), \quad (11)$$

and sensitivity roll-off is modeled as

$$W_{\text{roll}}(z) = \cos^4\left(\frac{\pi z}{z_{\text{max}}}\right), \quad (12)$$

chosen to emulate typical depth-dependent sensitivity decay while providing a tunable attenuation profile. As implemented here, the roll-off can be further down-weighted beyond mid-range,

$$W_{\text{roll}}(z) \leftarrow \eta W_{\text{roll}}(z) \quad \text{for} \quad z > \frac{z_{\text{max}}}{2}, \quad \eta \in (0, 1), \quad (13)$$

and the final system-weighted OCT signal is computed by

$$R_{\text{sys}}(z, x) = R(z, x) W_{\text{conf}}(z) W_{\text{roll}}(z), \quad (14)$$

with a small floor $R_{\text{sys}}(z, x) \leftarrow \max(R_{\text{sys}}(z, x), w_{\min})$ to avoid complete signal collapse at large depths. The displayed B-scan is obtained by log compression and contrast normalization for visualization.

3. EXPERIMENTS AND RESULTS

3.1 Dataset Composition and Experimental Protocol

The proposed framework generates a synthetic corneal OCT dataset of 10,000 B-scans, comprising 8,000 healthy samples and 2,000 keratoconus-like samples produced via controlled geometry and optical-parameter perturbations. As illustrated in Fig. 5, each sample is packaged as a paired set including a simulated OCT B-scan, pixel-accurate five-layer segmentation masks, three optical-parameter maps (refractive index n , scattering coefficient μ_s , and anisotropy factor g), and the corresponding system-effect-modulated OCT signals (e.g., confocal/PSF gating and sensitivity roll-off). The experiments in this work are conducted on the healthy subset to establish a clean benchmarking protocol. For computational efficiency, both tasks use randomly sampled B-scans from the full dataset (healthy + keratoconus): reconstruction is trained/tested on 1,000/500 samples, and segmentation on 1,000/100 samples.

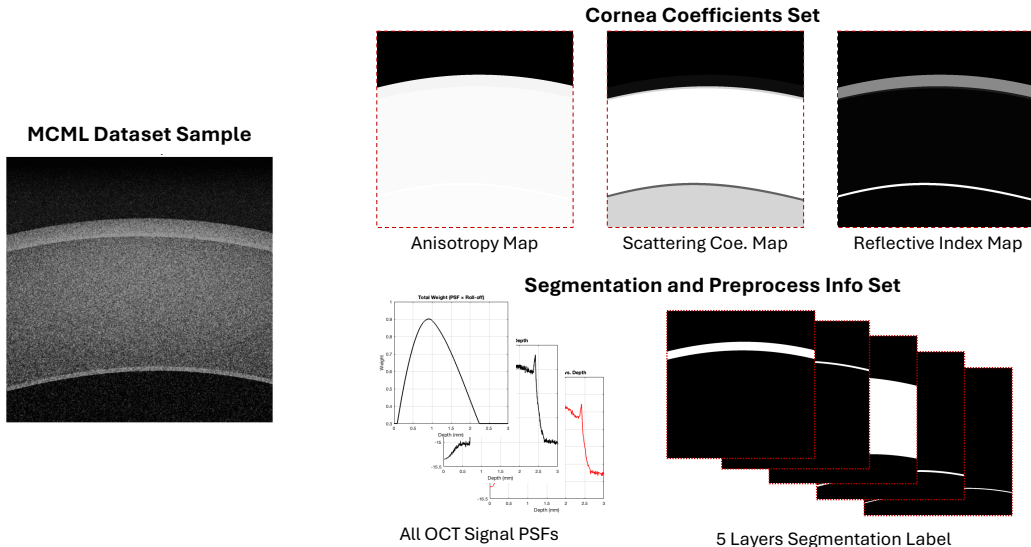


Figure 5. A representative sample set produced by the proposed framework.

3.2 Task I: Diffusion Benchmarking for Joint Optical-Map and Structural OCT Reconstruction

This experiment evaluates whether the proposed synthetic dataset can serve as a controlled benchmark for diffusion-based inverse OCT reconstruction under paired ground truth. Using healthy samples, the model takes a simulated raw OCT B-scan as input and jointly predicts three optical-parameter maps (n, μ_s, g) together with a structural OCT intensity output. A physics-based forward model is used during training to encourage signal-consistency between the predicted optical maps and the reconstructed OCT intensity. Performance is quantified using PSNR/SSIM/MSE for both the structural OCT output and the recovered parameter maps. Table 2 reports the quantitative comparison between the diffusion-based full model and a baseline U-Net. The diffusion model achieves markedly higher fidelity for structural OCT reconstruction and improved recovery of scattering-related parameters (μ_s and g), while the baseline remains competitive for refractive-index reconstruction. Figure 6 provides a representative qualitative comparison, where the diffusion model yields cleaner layer separation and more consistent parameter contrast across the corneal interfaces.

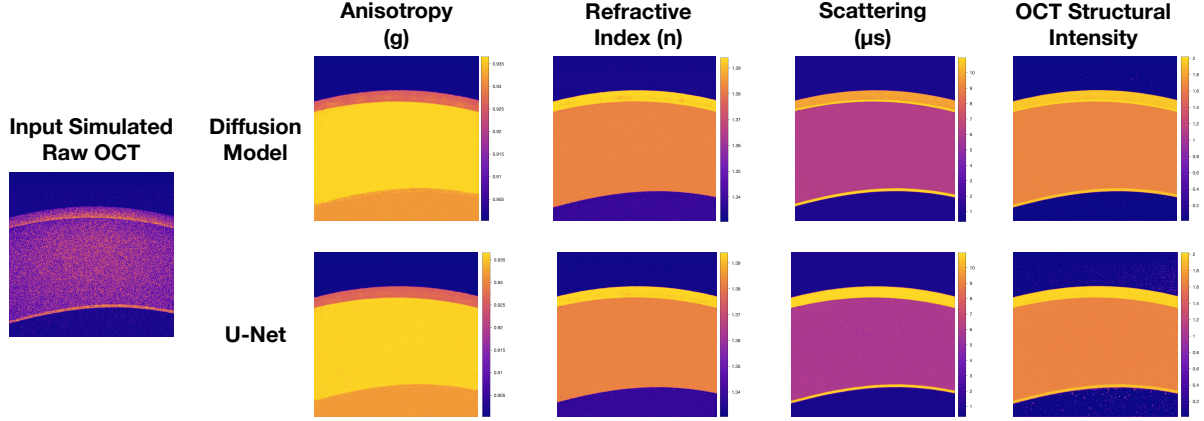


Figure 6. Qualitative comparison on a representative healthy sample for Task I.

Table 2. Task I results on healthy data for joint reconstruction. The Diffusion Model denotes the diffusion-based reconstruction approach, illustrating the dataset utility for diffusion benchmarking under paired ground truth.

Method	OCT			n		
	PSNR \uparrow	SSIM \uparrow	MSE \downarrow	PSNR \uparrow	SSIM \uparrow	MSE \downarrow
Diffusion Model	31.65	0.94	2.75e-3	28.76	0.66	6.54e-6
Baseline U-Net	25.04	0.85	1.2e-2	29.29	0.67	5.78e-6
Method	μ_s			g		
	PSNR \uparrow	SSIM \uparrow	MSE \downarrow	PSNR \uparrow	SSIM \uparrow	MSE \downarrow
Diffusion Model	28.03	0.70	0.23	29.25	0.84	1.90e-6
Baseline U-Net	24.09	0.63	0.56	27.89	0.78	2.60e-6

3.3 Task II: Baseline Evaluation for Three-Class Corneal Layer Segmentation

This experiment evaluates a simple segmentation baseline on the proposed synthetic corneal OCT dataset with pixel-accurate labels. To reduce task complexity and emphasize benchmarking utility, the original five corneal layers are merged into three classes: Epithelium (EPI), Bowman+Stroma (BS), and Descemet+Endothelium (DE). A vanilla U-Net is trained on healthy samples with a binary cross-entropy loss with logits and Adam optimization (learning rate 10^{-4}) for 200 epochs, using a random 9:1 train/test split.

Segmentation performance is quantified by per-class Intersection-over-Union (IoU) and mean squared error (MSE) on the held-out test set. As summarized in Table 3, the baseline achieves near-ceiling accuracy for BS and EPI, while DE remains comparatively more challenging. For qualitative assessment, as Fig. 7 shows, boundary curves are extracted from predicted masks by identifying per-column upper/lower interfaces and rendered as overlaid contours on the input OCT B-scan, enabling direct inspection of interface alignment and error patterns.

4. DISCUSSION AND CONCLUSION

The proposed method introduces a configurable physics-based pipeline for generating high-resolution synthetic corneal OCT B-scans with label-perfect supervision, directly addressing the data scarcity that limits training and stress-testing modern AI models. By combining Gaussian-parameterized multilayer geometry modeling with MCML and key system effects (confocal gating and sensitivity roll-off), the framework outputs paired OCT images, pixel-accurate five-layer masks, and aligned optical-parameter maps. The resulting dataset comprises 10,000 samples spanning healthy and keratoconus-like phenotypes, providing scalable data enlargement and controlled variation for reproducible training, ablation, and robustness evaluation.

Benchmarking on the healthy subset demonstrates two utilities for AI development: (i) in Task I, the diffusion-based reconstruction model substantially improves structural OCT fidelity and scattering-related parameter recovery over a baseline U-Net, showing that the dataset supports data-hungry generative inverse models with

Table 3. Task II mean segmentation performance on the held-out healthy test set (three merged classes).

Class	IoU \uparrow	MSE \downarrow
Bowman+Stroma (BS)	0.998865	5.99×10^{-4}
Descemet+Endothelium (DE)	0.980385	3.35×10^{-4}
Epithelium (EPI)	0.992192	4.50×10^{-4}

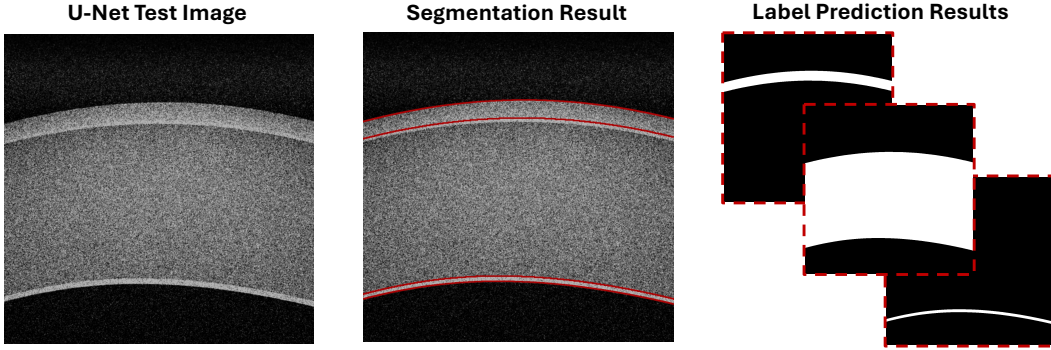


Figure 7. Qualitative assessment of three-class layer segmentation.

paired ground truth; and (ii) in Task II, a vanilla U-Net achieves near-ceiling IoU on merged three-class segmentation, validating geometric/label consistency and enabling fast, standardized baseline comparisons. Remaining gaps include simplified layer-wise optics and parametric system weighting; future work will incorporate richer scanner/noise effects and evaluate domain shift using the keratoconus subset to improve transfer to clinical OCT.

ACKNOWLEDGMENTS

This work was supported by National Institute of Biomedical Imaging and Bioengineering of the National Institutes of Health Grant under award number 1R01EY032127 (PI: Jin U. Kang). The study was conducted at Johns Hopkins University.

REFERENCES

- [1] Xu, J., Yu, J., Yao, J., and Zhang, R., “The neural networks-based needle detection for medical retinal surgery,” in [*International Conference on Computer Graphics, Artificial Intelligence, and Data Processing (ICCAID 2022)*], **12604**, 674–678, SPIE (2023).
- [2] Wang, Y., Singh, M. S., Li, K., Yu, J., Liu, X., and Kang, J. U., “Live porcine eye model studies of subretinal injection using handheld endoscopy oct integrated injector,” *Investigative Ophthalmology & Visual Science* **65**(7), 5499–5499 (2024).
- [3] Wang, Y., Opfermann, J., Yu, J., Yi, H., Kaluna, J., Biswas, R., Zuo, R., Gensheimer, W., Krieger, A., and Kang, J., “Reimagining partial thickness keratoplasty: An eye mountable robot for autonomous big bubble needle insertion,” *arXiv preprint arXiv:2410.14577* (2024).
- [4] Yu, J., Yi, H., Wang, Y., Opfermann, J. D., Gensheimer, W. G., Krieger, A., and Kang, J. U., “Topology-based deep-learning segmentation method for deep anterior lamellar keratoplasty (dalk) surgical guidance using m-mode oct data,” in [*Optical Fibers and Sensors for Medical Diagnostics, Treatment, and Environmental Applications XXV*], **13310**, 7–13, SPIE (2025).
- [5] Wang, Y., Guo, S., Opfermann, J. D., Kaluna, J., Gensheimer, B. G., Krieger, A., and Kang, J. U., “Common-path optical coherence tomography guided vertical pneumodissection for dalk,” in [*Optical Fibers and Sensors for Medical Diagnostics, Treatment and Environmental Applications XXIII*], **12372**, 15–19, SPIE (2023).
- [6] Gensheimer, W. G., Opfermann, J., Wang, Y., Kaluna, J., Krieger, A., and Kang, J. U., “Comparison of vertical cannula insertion techniques for big bubble deep anterior lamellar keratoplasty,” *Investigative Ophthalmology & Visual Science* **65**(7), 3700–3700 (2024).

- [7] Titiyal, J. S., Kaur, M., and Falera, R., “Intraoperative optical coherence tomography in anterior segment surgeries,” *Indian Journal of Ophthalmology* **65**(2), 116–121 (2017).
- [8] Wang, Y., Yu, J., Guo, W., Sun, Y., and Kang, J. U., “Super-resolution optical coherence tomography using diffusion model-based plug-and-play priors,” *arXiv preprint arXiv:2505.14916* (2025).
- [9] Guo, W., Yu, J., Wang, Y., Kang, J. U., and Sun, Y., “Psi3d: Plug-and-play 3d stochastic inference with slice-wise latent diffusion prior,” *arXiv preprint arXiv: 2512.18367* (2025).
- [10] Win, K. Y., Fai, J. W. H., Ying, W. Q., Qi, C. C. S., Chua, J., Wong, D., Ang, M., Schmetterer, L., and Tan, B., “Corneal layer segmentation in healthy and pathological eyes: A joint super-resolution generative adversarial network and adaptive graph theory approach,” *Translational Vision Science & Technology* **14**(3), 19–19 (2025).
- [11] Tripathi, A., Kumar, P., Mayya, V., and Tulsani, A., “Generating oct b-scan dme images using optimized generative adversarial networks (gans),” *Heliyon* **9**(8) (2023).
- [12] Zheng, C., Xie, X., Zhou, K., Chen, B., Chen, J., Ye, H., Li, W., Qiao, T., Gao, S., Yang, J., et al., “Assessment of generative adversarial networks model for synthetic optical coherence tomography images of retinal disorders,” *Translational Vision Science & Technology* **9**(2), 29–29 (2020).
- [13] Brenner, T., Munro, P. R., Krüger, B., and Kienle, A., “Two-dimensional simulation of optical coherence tomography images,” *Scientific Reports* **9**(1), 12189 (2019).
- [14] Guo, S. and Kang, J. U., “Convolutional neural network-based common-path optical coherence tomography a-scan boundary-tracking training and validation using a parallel monte carlo synthetic dataset,” *Optics Express* **30**(14), 25876–25890 (2022).
- [15] Yao, G. and Wang, L. V., “Monte carlo simulation of an optical coherence tomography signal in homogeneous turbid media,” *Physics in Medicine & Biology* **44**(9), 2307 (1999).
- [16] Wang, L., Jacques, S. L., and Zheng, L., “MCML—Monte Carlo modeling of light transport in multi-layered tissues,” *Computer Methods and Programs in Biomedicine* **47**(2), 131–146 (1995).
- [17] Sun, Y., Maimaiti, N., Xu, P., Jin, P., Cai, J., Qian, G., Chen, P., Xu, M., Jia, G., Wu, Q., et al., “An as-oct image dataset for deep learning-enabled segmentation and 3d reconstruction for keratitis,” *Scientific Data* **11**(1), 627 (2024).
- [18] Heslinga, F. G., Lucassen, R. T., van den Berg, M. A., van der Hoek, L., Pluim, J. P., Cabrerizo, J., Alberti, M., and Veta, M., “Corneal pachymetry by as-oct after descemet’s membrane endothelial keratoplasty,” *Scientific Reports* **11**(1), 13976 (2021).
- [19] Wang, J., Simpson, T. L., and Fonn, D., “Objective measurements of corneal light-backscatter during corneal swelling, by optical coherence tomography,” *Investigative Ophthalmology & Visual Science* **45**(10), 3493–3498 (2004).
- [20] Boettner, E. A. and Wolter, J. R., “Transmission of the ocular media,” *Investigative Ophthalmology & Visual Science* **1**(6), 776–783 (1962).
- [21] Meek, K. M. and Knupp, C., “Corneal structure and transparency,” *Progress in Retinal and Eye Research* **49**, 1–16 (2015).
- [22] Tuchin, V. V., “Tissue optics and photonics: biological tissue structures,” *Journal of Biomedical Photonics & Engineering* **1**(1), 3–21 (2015).
- [23] Bashkatov, A. N., Berezin, K. V., Dvoretskiy, K. N., Chernavina, M. L., Genina, E. A., Genin, V. D., Kochubey, V. I., Lazareva, E. N., Pravdin, A. B., Shvachkina, M. E., et al., “Measurement of tissue optical properties in the context of tissue optical clearing,” *Journal of Biomedical Optics* **23**(9), 091416–091416 (2018).